Optical properties of V-groove silicon nitride trench waveguides

QIANCHENG ZHAO, YUEWANG HUANG, AND OZDAL BOYRAZ*

Department of Electrical Engineering and Computer Science, University of California, Irvine, California 92697, USA
Corresponding author: oboyraz@uci.edu

We numerically investigate the mode properties of the V-groove silicon nitride trench waveguides based on the experimental results. The trench waveguides are suitable for nonlinear applications. By manipulating the waveguide thicknesses, the waveguides can achieve zero dispersion or a maximized nonlinear parameter of $0.219 \ \mathrm{W^{-1} \cdot m^{-1}}$ at 1550 nm. Broadband four-wave mixing with a gain of $5.545 \ \mathrm{m^{-1}}$ is presented as an example. The waveguides can also be applied in sensing applications with an optimized evanescent intensity ratio. By etching away the top flat slabs, wider trapezoidal trench waveguides can be utilized for plasmonic sensing thanks to their TE fundamental modes.   © 2016 Optical Society of America

1. INTRODUCTION

Trench waveguides are built on channels, with their guiding regions below the substrate surface. Silicon can be used as the substrate material to provide V-groove trenches that are fabricated by anisotropic etching [1–5]. Trench waveguides built on V-grooves first emerged in 1970s with bilayer configurations. The first layer deposited on the silicon substrate has a lower refractive index to serve as the cladding, and the second layer with a higher refractive index is deposited on top of the first layer and sometimes etched to confine the light. Different wave guiding materials have been studied, such as epoxy [6], plastic [7,8], glass [9,10], and polymer [11,12]. These earlier works were all passive devices, mainly aiming to lower the propagation loss, to improve the fiber to waveguide coupling coefficient, and to redirect light. Since the first demonstration of the E7 nematic liquid crystal channel waveguide in SiO_2-Si V-grooves [13], there has been a thrust in using liquid crystals as the guiding material in the V-groove [14–18] or semicircular groove [19] trench waveguides as potential candidates for low-cost, highly functional photonic elements. The liquid crystals, whose optical properties rely on the applied voltage, are encapsulated by the grooves and the indium-tin-oxide layer, forming a microscale triangle channel waveguide for electro-optical modulation. Although widely employed as passive and active devices, all the previously studied trench waveguides had large cross sections, which are incompatible with nanophotonics. For nanophotonics, it is preferable to find a fabrication method that is scalable and reliable. The V-groove trench waveguide has been reexamined in the field of nanophotonics due to its capability of controlling the sidewall angles and the self-stopping etching feature in triangle waveguides. Recently, sub-micron silicon nitride trench waveguides have been fabricated using microelectromechanical-systems (MEMS)-grade optical lithography [20]. The waveguide exhibits a nonlinear effect that is 100 times greater than that of single-mode fibers and that benefits from the tight mode confinement, group velocity dispersion management, and low propagation loss.

The interest in using V-groove trench waveguides lies in but is not limited to the following reasons: (i) the surface roughness on the sidewall is smoothened by the preferential etching process on silicon, (ii) the high degree precision ensured by self-aligning obtained from anisotropic etching at a low cost, (iii) the large-area production of sub-micron features, and (iv) the inborn advantage of combining photonics and microfluidics with the help of the V-groove channels. These features render the V-groove trench waveguides suitable in low-loss, high-confinement, and optofluidic applications. In our recent work, the measured propagation loss of the silicon nitride trench waveguides was as low as 0.8 dB/cm with a nonlinear parameter $\gamma = 0.3 \ \mathrm{W^{-1} \cdot m^{-1}}$ [20]. Gold nanoparticles can be deposited on the trench waveguide to further boost the nonlinearity [21]. Trench waveguides can also be used in optical trapping applications with the help of plasmonic bowtie antennas [22].

Solving the mode solutions for the trench waveguides is the fundamental step to understand the optical properties that are determined by the trench waveguide structures. The cross sections of these waveguides are irregular, with their core regions varying from triangle to trapezoidal shapes. In the past,

theoretical analyses based on the finite element method (FEM) [23], the effective index method [24], the Rayleigh principle and least-squares method [25], and the weighted residual method [26] have been put forward to study the mode properties in trapezoidal waveguides. However, the conclusions drawn from those analyses cannot be generalized for all the trench waveguides because the wave guiding layer is non-flat. Therefore, the waveguides need to be examined thoroughly to unveil their optical properties.

Preliminary studies on the optical properties of trench waveguides have been investigated in our previous work [27]. However, deeper study needs to be continued to identify the interplay among the waveguide geometries, mode leakage, evanescent intensity ratio (EIR), and nonlinear parameters. The mode leakage study guarantees low-loss wave propagation. The EIR quantitatively characterizes the light-matter interaction, which is the key to optical sensing. In our previous papers [20,27], we used Bezier curves to model the rounding effect on the sidewalls. However, such an approach is not scalable and is insufficient for a comprehensive study with different geometries. In this study, we provide arcs to represent rounding edges and show that we can generalize modeling for different geometries. As a result, the mode distributions, the EIR, and the dispersions based on the new model are extended for waveguide geometries with widths up to 5 μm. Moreover, besides the linear properties, the geometric effects on the nonlinear properties are added in this paper. By tailoring the geometric parameters, trench waveguides with small mode areas, large nonlinear parameters, and low group velocity dispersion can be used in nonlinear applications. The waveguides can have zero dispersion at 1550 nm or a maximized nonlinear parameter of $0.219 \ \mathrm{W^{-1} \cdot m^{-1}}$ at 1550 nm by manipulating their waveguide thicknesses. An in-depth study reveals that the triangle trench waveguide is suitable for broadband four-wave mixing (FWM) with a maximum gain of $5.545 \ \mathrm{m^{-1}}$ in a degenerate configuration. The group velocity dispersion at the pump wavelength 1.44 μm is $2.15 \ \mathrm{ps \cdot nm^{-1} \cdot km^{-1}}$ with a dispersion slope of $-1.725 \times 10^{-2} \ \mathrm{ps \cdot nm^{-2} \cdot km^{-1}}$. Narrow-band FWM can also be realized at 1550 nm, with a maximum gain of $0.13 \ \mathrm{m^{-1}}$. Unlike our previous waveguide structure, we also introduce a new geometry with the top slabs etched away to improve the mode confinement and to utilize the TE mode for plasmonic sensing applications. The novelty of this paper is to provide a comprehensive and systematic numerical study of the linear and nonlinear mode properties of V-groove trench waveguides for the first time to our knowledge.

This paper is organized as follows. The fabrication procedure will be briefly introduced in Section 2. Then, starting from the mode polarization properties of the waveguides, we investigate the leakage of the waveguide caused by the top slab regions. The nonlinear properties and group velocity dispersions are presented, followed by the EIR study, in Section 3. In Section 4, an improved silicon nitride trench waveguide structure is introduced to reduce the mode leakage, and its usage is discussed in plasmonic antenna-assisted sensing applications. Finally, the conclusion will summarize trench waveguide properties.

2. TRENCH WAVEGUIDE FABRICATION

Fabrication of the V-groove trench waveguides does not require E-beam lithography, but merely relies on optical lithography followed by anisotropic potassium hydroxide etching. Using this method, even sub-micron waveguide dimension can be achieved with a MEMS-grade photomask. The anisotropic potassium hydroxide (KOH) etching on a ⟨100⟩ silicon wafer carves a trapezoidal or triangular trench with an angle of 54.7° with respect to the substrate surface. The shape of the waveguide is determined by the etching depth H, the opening window width W_{open}, and the silicon nitride deposition thickness T_{SiN}. In Fig. 1, we show two waveguides with their bottom regions being triangle or trapezoidal shapes. The two trench waveguides have the same etching depth of 3 μm, but their values of W_{open} are 4 and 5 μm in Figs. 1(a) and 1(b), respectively. Low-pressure chemical vapor deposition (LPCVD) was used to deposit a $T_{\mathrm{SiN}} = 725$ nm layer of silicon nitride in two cycles. The detailed fabrication procedure can be found in Ref. [20].

The variation of the waveguide width and thickness affects the waveguide propagation properties and the mode distributions. The waveguides propagation losses were experimentally measured using a cut-back method for both the TE (electric field along the x-axis) and the TM (electric field along the y-axis) modes at 1550 nm [28]. The propagation loss is as low as 0.8 ± 0.26 dB for the TM mode in the trench waveguide with $W_{\mathrm{open}} = 5$ μm. For its TE mode, it is 3.13 ± 0.37 dB/cm. In the trench waveguide with $W_{\mathrm{open}} = 4$ μm, the propagation losses for the TM and TE modes are 1.66 ± 0.42 dB/cm and 4.5 ± 0.34 dB/cm, respectively. We also experimentally tested the nonlinear refractive index n_2 of the guiding material to be $1.39 \times 10^{-19} \ \mathrm{m^2/W}$ [20,28].

3. NUMERICAL ANALYSIS

A. Numerical Model

The theoretical model, based on Fig. 1(b), is redrawn in Fig. 2. The sidewall angle θ of the waveguide is 54.7°, consistent with the silicon wet etching properties. Unlike our preliminary model that used Bezier curves [20,27], the connections between the silicon nitride sidewalls and top flat slabs are smoothed with arcs of $r_1 = 2$ μm and $r_2 = 2$ μm + T_{SiN} to mimic the actual fabrication images. The size of the trench waveguide is characterized by the waveguide bottom width W_{btm} and the actual waveguide thickness T. W_{btm} and T can be derived from the fabrication parameters, W_{open}, H,
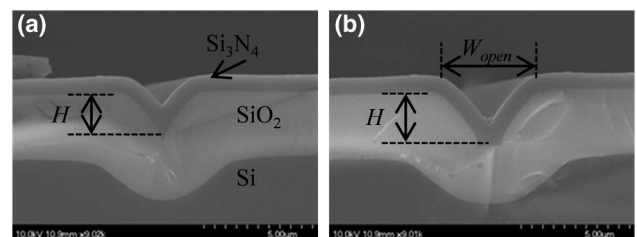

Fig. 1. SEM images for fabricated silicon nitride trench waveguides with thickness $T_{\mathrm{SiN}} = 725$ nm, etching depth $H = 3$ μm, and top opening window (a) $W_{\mathrm{open}} = 4$ μm and (b) $W_{\mathrm{open}} = 5$ μm.
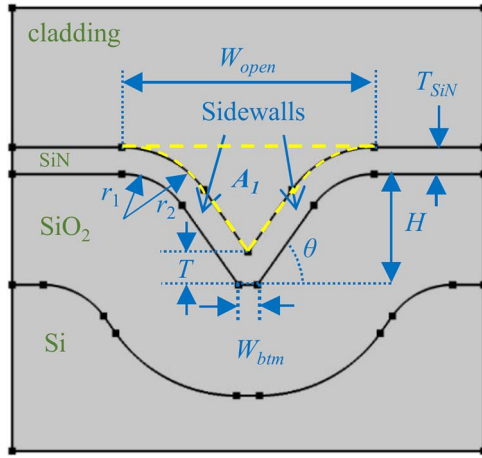
Fig. 2.   Silicon nitride trench waveguide cross section. The region surrounded by the yellow dashed line is the sensing region, and the area of this region is A_1. The total simulation area is denoted as A_{tot}.

and T_{SiN}. For example, W_{btm} is governed by $W_{btm} = W_{open} - 2 \cot(\theta) \cdot H$. If $W_{open} < 2 \cot(\theta) \cdot H$, W_{btm} will be 0, and a triangle trench will be carved out, shown in Fig. 1(a). Otherwise, the trenches will be trapezoidal, as shown in Fig. 1(b). The actual waveguide thickness T is affected by the silicon nitride deposition process, which grows faster in corners. T has the following relation with the silicon nitride deposition thickness T_{SiN} and the waveguide bottom width W_{btm}:

$$\begin{cases} T = T_{SiN}, & \text{if } W_{btm} \geq 2 T_{SiN} \tan\left(\frac{\theta}{2}\right) \\ T = \frac{T_{SiN}}{\cos(\theta)} - \frac{W_{btm}}{2} \tan(\theta), & \text{if } W_{btm} < 2 T_{SiN} \tan\left(\frac{\theta}{2}\right) \end{cases} \quad \textbf{(1)}$$

In our simulations, H and T_{SiN} are set to be 3 and 0.725 μm based on the fabrication results. It is worth mentioning that the shapes of the real devices may not follow Eq. (1) strictly due to imperfect fabrication, and this may affect the optical mode properties. For example, the $W_{open} = 5$ μm waveguide has less propagation loss than the waveguide with $W_{open} = 4$ μm in Fig. 1, because the thickness T in the $W_{open} = 5$ μm waveguide is thicker than expected [20], making the mode guide better. The irregularity in the trench's bottom region depends on the fabrication process and may vary from device to device. Therefore, it is difficult to abstract and generalize the deformation into a simple geometric model. However, using straight lines in the trenches without considering the deformation greatly simplifies the structure without losing the representativeness, and the approach has also been used in other literature, e.g., Ref. [14]. Thus, the theoretical mode is still accurate in characterizing the mode properties.

The simulations are carried out in a frequency-domain FEM solver (COMSOL Multiphysics). The refractive index of the low-stress silicon nitride is a function of the wavelength and is defined as $n^2(\lambda) = 1 + 3.585\lambda^2/(\lambda^2 - 0.1316^2)$ [20], where λ is in units of micrometers. The refractive index of SiO_2 is adopted from Ref. [29]. Perfectly matched layer boundary conditions are used to minimize the backscattering at the boundaries. All the simulations are performed at the telecommunication wavelength 1550 nm unless otherwise specified.

B. Mode Distribution

The trench waveguide has its modes guided in the core region. Due to the inclined sidewalls, it does not support pure the TE or TM modes that are commonly found in rectangular waveguides. Instead, its modes are hybrid and have both x and y components. The fundamental mode of a triangle trench waveguide ($W_{btm} = 0$) is a quasi-TM mode with a TM fraction of 82.0%. The TM fraction is defined as

$$\frac{\iint |E_y|^2 \mathrm{d}x\mathrm{d}y}{\iint (|E_x|^2 + |E_y|^2)\mathrm{d}x\mathrm{d}y}. \quad \textbf{(2)}$$

The TE fraction can be defined in a similar way by changing E_y with E_x in the numerator. Figure 3 shows the quasi-TM and quasi-TE modes of a triangle trench waveguide ($W_{btm} = 0$). The quasi-TE mode has a TE fraction of 73.4%. These mode distributions have a large impact on the losses experienced by the pure TE and TM modes. For instance, the waveguide with $W_{open} = 4$ μm has a propagation loss of 1.66 ± 0.42 dB/cm for the quasi-TM mode and of 4.5 ± 0.34 dB/cm for the quasi-TE mode. Three-dimensional simulations show that the mode shape is preserved along the waveguide, which means the loss of the hybrid modes is a combination of the individual polarization components. Based on these measurements and the simulations, we can estimate the losses experienced by the pure TM and TE modes are 1.03 and 7.04 dB/cm, respectively. It is also worth noting that since quasi-TE modes have larger mode areas (will be proven later), they will be more susceptible to fabrication intolerances and surface roughness, as indicated by the experimental measurements.

As can be seen from the mode profiles, the trench waveguide is analogous to a rib waveguide in the way that the trench's bottom region provides a higher effective refractive index than the sidewalls and the top slabs. In other words, the guiding mechanism in the waveguide relies on the effective refractive index difference between the trench's bottom region and the adjacent slabs. Due to the silicon nitride deposition property, the trench's bottom region is thicker than the slab regions when the trench waveguide is narrow; thereby, the bottom region has a higher local effective refractive index. In particular, the triangle trench waveguide has the largest thickness as $T_{SiN}/\cos(\theta)$. According to Eq. (1), as W_{btm} increases, T decreases, and finally becomes equal to T_{SiN}, resulting in a reduction in the effective refractive index difference and causing the modes to leak into the slab regions. The change of W_{btm} will affect the mode properties. Figures 3(a) and 3(b) show the
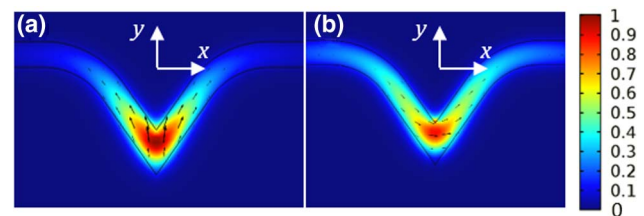

Fig. 3.   (a) Normalized quasi-TM mode and (b) normalized quasi-TE mode profile in a triangle trench waveguide. The black arrows represent the electric fields.

effective refractive indices (n_{eff}) and effective mode areas (A_{eff}) of the quasi-TM and quasi-TE modes as a function of W_{btm}. As the W_{btm} increases from 0 to 0.7 μm, the A_{eff} expands from 2.8 to 6.7 μm^2 for quasi-TM mode and from 4.1 to 8.9 μm^2 for quasi-TE mode. n_{eff} for the quasi-TM mode drops more quickly than that for the quasi-TE mode because guiding the quasi-TM mode relies more on the layer thickness in the trench bottom. The value of n_{eff} drops while A_{eff} increases as W_{btm} increases, indicating the mode guidance is weakened when the waveguide becomes wide. Figures 3(c) and 3(d) particularly compare the normalized quasi-TM electric field profiles of a triangle trench waveguide with $W_{\text{btm}} = 0$ and a trapezoidal trench waveguide with $W_{\text{btm}} = 0.7$ μm. In terms of better confinement and low-loss propagation applications, one should target the triangle trench waveguides.

C. Waveguide Nonlinear Coefficient and Dispersion

Silicon nitride can be used in nonlinear applications because of the absence of two-photon absorption and free carrier absorption [30]. Waveguides made of silicon nitride can be designed to have a high effective nonlinear parameter γ [31], which is defined as $\gamma = (2\pi n_2)/(\lambda A_{\text{eff}})$ [32]. Here, the nonlinear refractive index n_2 is fixed by the uniform guiding layer of silicon nitride, but A_{eff} can be varied by adjusting the waveguide geometry and wavelength to facilitate a large effective nonlinearity γ.

We measured a nonlinear index n_2 of 1.39×10^{-19} m^2/W for low-stress silicon nitride waveguides in our previous work [20]. Our value is compared with other experimental results at telecommunication wavelengths from different waveguide dimensions in Table 1. In addition, the values of n_2 of SiO$_2$ and Si are also added as reference values. Our measured value falls among the others as shown in Table 1, which is anticipated by taking the waveguide geometry and material properties into considerations. On the one hand, low confinement waveguides have more power extending in the SiO$_2$ cladding region, leading to a lower effective n_2. On the other hand, increasing the silicon content results in an increase in the material nonlinearity.

Nonlinear effects can occur over a broad spectrum range. Both A_{eff} and n_2 are functions of λ, and so is γ. The dispersion of n_2 over the wavelength can be estimated accurately based on the linear refractive indices by using Miller's rule [37],

$$n_2(\text{SI}) = k \frac{40\pi^2}{cn^2(\lambda)} \chi^{(3)} \ (\text{esu}), \tag{3}$$

$$\chi^{(3)} \ (\text{esu}) = [\chi^{(1)} \ (\text{esu})]^4 \times 10^{-10}, \tag{4}$$

$$n^2(\lambda) = 1 + 4\pi\chi^{(1)} \ (\text{esu}), \tag{5}$$

where c is the speed of light, $n(\lambda)$ is the wavelength-dependent refractive index in SI units and is given in Section 3.A, $\chi^{(1)}$ is the first-order susceptibility, and $\chi^{(3)}$ is the third-order susceptibility. Both $\chi^{(1)}$ and $\chi^{(3)}$ are in electrostatic units, and k is a parameter to fit the experimental results and is estimated to be 0.7143 in our calculations.

As illustrated in Fig. 4(b), for a trench waveguide with a fixed thickness, it has the smallest A_{eff} when $W_{\text{btm}} = 0$, which is in favor of nonlinear applications. Therefore, we give priority to considering the triangle trench waveguides for nonlinear applications. Given the n_2 for SiO$_2$ from the literature and the calculated n_2 for silicon nitride in the wavelength range from 1.35 to 1.65 μm, the nonlinear parameter γ has been simulated for trench waveguides with different deposition thicknesses over the spectrum range, as presented in Fig. 5(a), which shows the results for the quasi-TM mode in triangle trench waveguides with air cladding. The trench waveguides have a higher γ at shorter wavelengths. Waveguides with T_{SiN} between 400 and 700 nm have a larger γ due to the tight mode confinement. The largest γ is 0.327 W^{-1} m^{-1} when $T_{\text{SiN}} = 540$ nm at wavelength of 1350 nm. At a 1550 nm wavelength, γ is maximized to be 0.219 W^{-1} m^{-1} when $T_{\text{SiN}} = 600$ nm.

In nonlinear applications, the phase mismatch will limit the efficiency of the nonlinear process. To obtain phase matching for broadband wavelength conversion, the waveguide dispersion D should be engineered by tailoring the waveguide dimensions, so that the pump wavelength is in the anomalous region and close to the zero-dispersion wavelength. To study the dispersion of the waveguides, we simulate the effective refractive index n_{eff} for various wavelengths, which takes both the material dispersion and the waveguide dispersion into
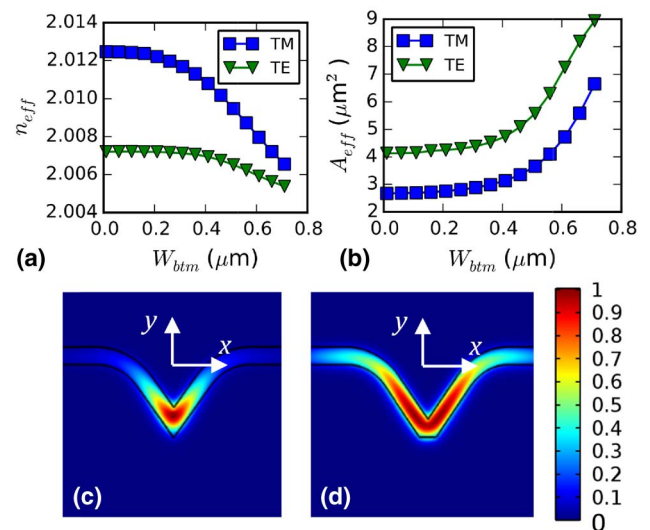
Table 1. Comparison of Nonlinear Kerr Coefficient n_2 for Silicon Nitride Waveguides with Different Fabrication Methods and Waveguide Geometries

	n_2 (m^2/W)	Geometry
SiO$_2$ [33]	2.16×10^{-20}	Optical fibers
Si$_3$N$_4$ (LPCVD) [34]	9×10^{-20}	2.8 μm × 80 nm
Si$_x$N$_y$ (LPCVD) [20]	1.39×10^{-19}	Trench waveguide
Si$_3$N$_4$ (PECVD) [31]	2.4×10^{-19}	1 μm × 500 nm
Si$_x$N$_y$ (LPCVD) [35]	1.4×10^{-18}	1.65 μm × 700 nm
Si [36]	4×10^{-18}	Bulk crystalline Si

Fig. 4. (a) n_{eff} and (b) A_{eff} of the quasi-TM and quasi-TE modes as a function of W_{btm}. The normalized quasi-TM electric field profiles of a triangle trench waveguide with (c) $W_{\text{btm}} = 0$ and with (d) $W_{\text{btm}} = 0.7$ μm.
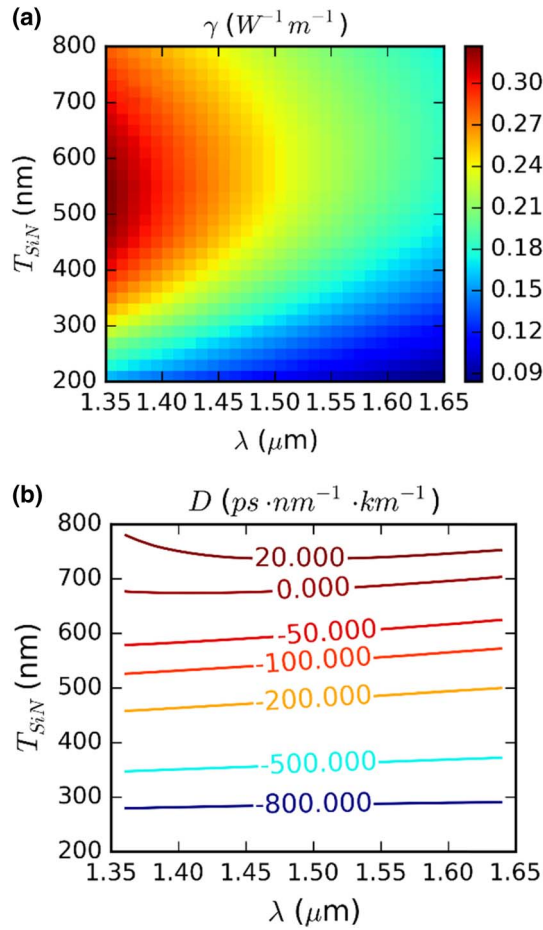
Fig. 5. (a) Simulation of the nonlinear parameter γ as a function of the silicon nitride deposition thickness T_{SiN} and the wavelength λ for the fundamental quasi-TM modes in the trench waveguides with $W_{btm} = 0$ and air cladding. (b) Simulation of dispersion D as a function of silicon nitride deposition thickness T_{SiN} and wavelength for the fundamental quasi-TM mode in trench waveguides with $W_{btm} = 0$ and air cladding.

consideration. Our simulation results presented in Fig. 5(b) show that the dispersion D can be tuned from –800 to 20 ps · nm^{-1} · km^{-1} by changing T_{SiN} from 280 to 800 nm. Thick silicon nitride trench waveguides ($T_{SiN} > 670$ nm) can have their dispersion in the anomalous region and close to zero, which is in agreement with the experimental work in Ref. [38]. However, growing thick silicon nitride films will be subject to a film cracking risk due to the tensile stress [39], and hence, multiple deposition and annealing steps may be required. The waveguide with $T_{SiN} = 687$ nm has zero dispersion at 1550 nm, with a zero-dispersion slope of 8×10^{-2} ps · nm^{-2} · km^{-1}. Close scrutiny on the simulation results predicts that FWM may be efficient in the triangle trench waveguide with $T_{SiN} = 680$ nm. For this geometry, the group velocity dispersion at the pump wavelength at the E-band (near 1450 nm) is close to 2.15 ps · nm^{-1} · km^{-1}, with a dispersion slope of -1.725×10^{-2} ps · nm^{-2} · km^{-1}. If one chooses the pump wavelength λ_2 to be 1.44 μm, the pump wavelength will be in the anomalous region and stay close to zero. For the degenerate FWM with Stokes and anti-Stokes wavelengths

at $\lambda_3 = 1.53$ μm and $\lambda_1 = 1.36$ μm, respectively, the phase mismatch will be $\Delta k = \beta_1 + \beta_3 - 2\beta_2 = 11.09$ m^{-1}. Correspondingly, the maximum parametric gain is $g_{max} = \gamma P_0 = \Delta k/2 = 5.545$ m^{-1} with undepleted pump approximation [28], where P_0 is the peak pump power at the input of the waveguide. Given the nonlinear parameter $\gamma = 0.2597$ W^{-1} m^{-1} at the pump wavelength, P_0 should be around 21.4 W, which is easily attainable by using mode-locked lasers. The peak power level is safe for silicon nitride waveguides. Similar or even larger peak powers have already been used in silicon nitride waveguides [30,40]. Such wavelength converters are particularly useful for frequency band conversion between the C-band and the E-band. Besides broadband FWM, the same waveguide can also be used for narrow-band FWM within the C-band, where $\lambda_1 = 1.54$ μm, $\lambda_2 = 1.55$ μm, and $\lambda_3 = 1.5613$ μm. This configuration yields a maximum parametric gain of 0.13 m^{-1} with $\gamma = 0.215$ W^{-1} m^{-1} and $P_0 = 604$ mW at a 1550 nm pump wavelength. In this calculation, we assume there is no loss. However, in the presence of loss, the parametric gain will be reduced due to a reduction of the pump power. The influence of the loss can be reflected from the effective length of the waveguide that is expressed as $L_{eff} = (1 - \exp(-\alpha L))/\alpha$, where L is the waveguide length, and α is the propagation loss (m^{-1}). For example, the propagation loss for the TM mode in the triangle trench waveguides with $T_{SiN} = 725$ nm was measured to be 1.66 dB/cm [28]. Correspondingly, the effective length for a 2 cm-long waveguide is only 1.4 cm.

In addition to changing the waveguide thickness, varying the trench waveguide width is an attractive approach to manipulating the waveguide dispersion because it is more practical in the actual fabrication. Quasi-phase matching can be achieved by alternating the waveguide width to compensate for the phase mismatch [41,42]. The concept can also be applied in the trench waveguides. Figure 6 presents the dispersion D as a function of W_{btm} for the trench waveguide with $T_{SiN} = 700$ nm and $H = 3$ μm at 1550 nm. The waveguide has zero dispersion when $W_{btm} = 0.34$ μm. Below that value, the waveguide is in the anomalous dispersion region, and above that, the waveguide is in the normal dispersion region.

D. Evanescent Intensity Ratio

The trench waveguide has an inborn advantage for sensing, because the trench valley can work as a container for liquids. Therefore, we did not deposit any cap layer on top of the silicon
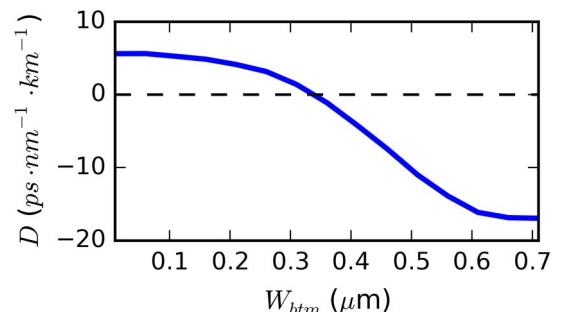

Fig. 6. Group velocity dispersion D as a function of W_{btm} for the trench waveguide with $T_{SiN} = 700$ nm and $H = 3$ μm.

nitride guiding layer. The evanescent fields from the core region directly interact with the analyte in the sensing region (enclosed by the yellow dashed line in Fig. 2). The more evanescent field extending into the sensing region, the more light-matter interactions there will be. To quantify the evanescent field strength, we define the evanescent intensity ratio EIR as

$$\text{EIR} = \frac{\iint_{A_1} |E(x,y)|^2 dx dy}{\iint_{A_{\text{tot}}} |E(x,y)|^2 dx dy}, \qquad (6)$$

where A_1 is the area of the trench channel, and A_{tot} is the total simulation area, which includes A_1. EIR highly depends on the waveguide geometry, in particular on the width of the waveguide bottom, W_{btm}, the deposition thickness of the silicon nitride, T_{SiN}, the polarization state of the light, and the refractive index of the upper cladding layer. For instance, the EIR dependency on W_{btm} is presented in Fig. 7. In this study, we assess the polarization and geometry dependence of EIR for a trench waveguide with $T_{\text{SiN}} = 725$ nm and $H = 3$ µm. As W_{btm} increases from 0 to 0.7 µm, the EIR for the quasi-TE mode decreases from 2.26% to 1.81% in an air-cladding waveguide, and from 3.04% to 2.57% in a water-cladding waveguide. On the contrary, the EIR for the quasi-TM mode increases and reaches peak values of 3.17% in the water-cladding waveguide when $W_{\text{btm}} = 0.56$ µm and 2.35% in the air-cladding waveguide when $W_{\text{btm}} = 0.51$ µm. The variation in EIR with respect to the cladding material is expected. Water cladding gives a larger EIR than air cladding due to its lower index contrast. Thus, for sensing applications, $W_{\text{btm}} = 0.56$ µm is an optimum value for a water-cladding trench waveguide with $T_{\text{SiN}} = 725$ nm.

The waveguide thickness will also affect the EIR, and the impact is illustrated in Fig. 8. In these studies, the cladding is set to be water and H is set to be 3 µm. The legends represent the deposition thickness T_{SiN} instead of the actual core region thickness T. The variation of the waveguide width is up to $W_{\text{btm}} = 2T_{\text{SiN}} \cdot \tan(\theta/2)$, beyond which the modes are leaky and the solutions are no longer accurate. The results indicate that thin waveguide has a larger EIR since more of the field is squeezed into the sensing region. Also, as illustrated, the EIR has a five-fold enhancement when T_{SiN} is reduced from 725 to 300 nm.
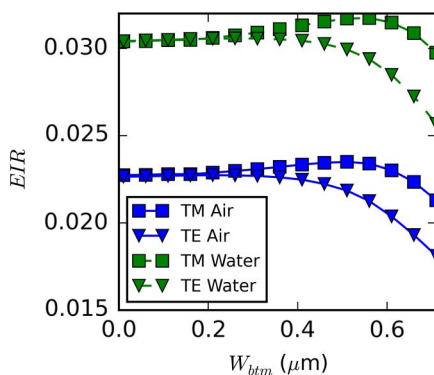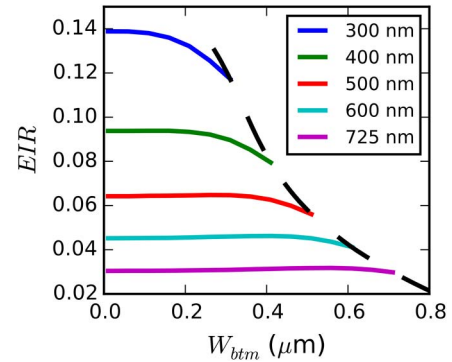

Fig. 8. EIR of the quasi-TM modes as a function of W_{btm} and T_{SiN}. The black dashed line represents the watershed where $W_{\text{btm}} = 2T_{\text{SiN}} \cdot \tan(\theta/2)$. The legends represent T_{SiN}.

4. IMPROVEMENTS ON MODE LEAKAGE

As stated in Section 3.B, the mode leakage into the top slab region limits the trench waveguide width. For instance, the bottom width of the waveguide with $T_{\text{SiN}} = 725$ nm should be smaller than 0.75 µm for the sake of low-loss mode confinement (<4 dB/cm). To get rid of the width restrictions, an improved trench waveguide structure is put forward in Fig. 9(b). By patterning and developing the photoresist (PR), the trench waveguide will undergo dry etching with its trench region protected by the PR strip. The top slab regions will be etched away, leaving only the trench's bottom part and the sidewalls.

Etching away the top slabs effectively improves the mode confinement in the trench waveguides. Compared with previous designs, the effective mode indices are purely real numbers in the new design, indicating no mode leakage from the waveguide. What is more, high-order modes emerge as a result of the good confinement in the improved waveguide. Those high-order modes cannot survive in the previous design because they have large imaginary mode indices, meaning high attenuation (>30 dB/cm). Close scrutiny on the effective mode indices shows that the fundamental mode for the wide ($W_{\text{btm}} > 0.9$ µm) trench waveguides is the TE mode, as presented in Fig. 10(a). When W_{btm} increases from 0, both the quasi-TM [Fig. 10(b)] and quasi-TE [Fig. 10(c)] mode refractive indices drop. This is caused by the drop of the trench thickness T, which weakens the lateral guidance. T is plotted with respect to W_{btm} as the black dashed line in Fig. 10(a). However, when W_{btm} exceeds 0.9 µm, the quasi-TE mode refractive index increases again and becomes the fundamental mode [Fig. 10(g)], whereas the quasi-TM mode evolves to be the sidewall mode [Fig. 10(f)]. Two high-order modes are also presented in Fig. 10, namely, hybrid-TE$_1$ [Fig. 10(h)] and

Fig. 7. EIR as a function of W_{btm} for a trench waveguide with $T_{\text{SiN}} = 725$ nm and $H = 3$ µm. The blue curves are for the waveguides with air cladding, while the green curves are for the waveguides with water cladding.
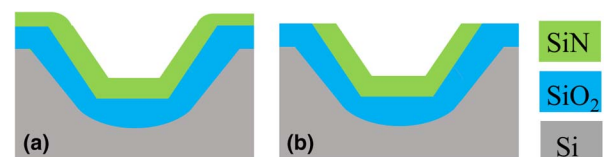

Fig. 9. (a) The cross section of the original trench waveguide. (b) The cross section of the trench waveguide with top etching.

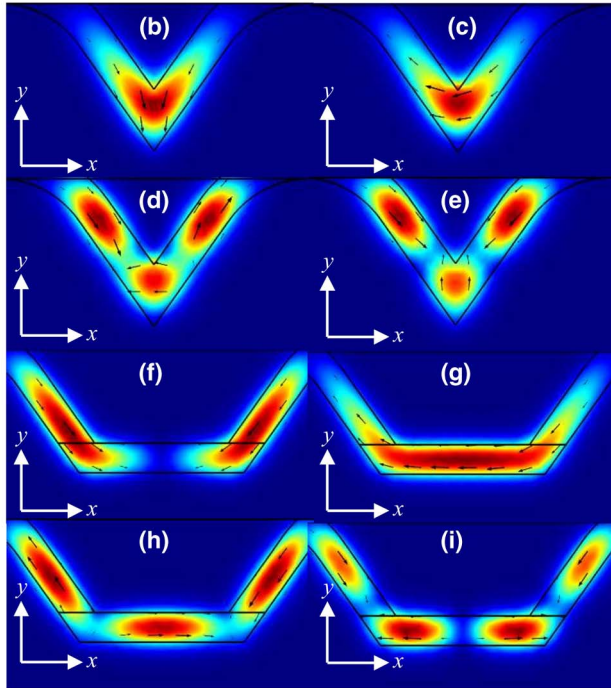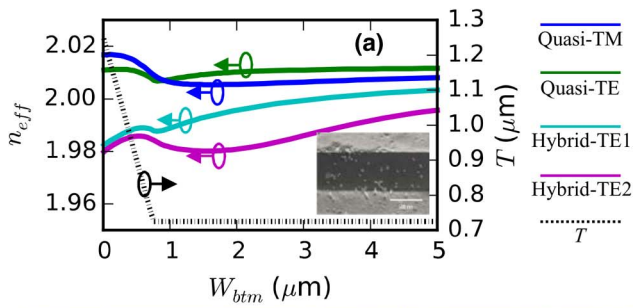**Fig. 11.** EIR of the waveguide fundamental mode as a function of W_{btm} in trench waveguides with $H = 3$ μm, $T_{SiN} = 725$ nm, and water cladding. The black dashed line shows the boundary between the quasi-TM and quasi-TE mode as the waveguide fundamental mode.

Fig. 10. (a) Effective refractive indices as a function of W_{btm} for a top-etched trench waveguide with $H = 3$ μm, $T_{SiN} = 725$ nm, and air cladding. The inset shows the SEM image of a trench waveguide coated with gold nanoparticles [21]. The scale bar of the SEM image is 500 nm. The field distributions of the quasi-TM mode (b), quasi-TE mode (c), hybrid-TE$_1$ mode (d), and hybrid-TE$_2$ mode (e) when $W_{btm} = 0$. The field distributions of the quasi-TM mode (or sidewall mode) (f), quasi-TE mode (g), hybrid-TE$_1$ mode (h), and hybrid-TE$_2$ mode (i) when $W_{btm} = 4$ μm. All the mode profiles have been normalized to their own maxima. The black arrows represent the electric fields.

hybrid-TE$_2$ [Fig. 10(i)]. "Hybrid-" means the mode has power at the base of the trench and at the sidewalls. The field at the trench's bottom region is polarized along the x-axis and can be classified as a TE mode. However, the field at the sidewalls include both x and y polarizations; therefore, the modes are considered as "hybrid-TE." The subscript of the modes is named after the number of the field peaks in the trench's bottom region. Although hybrid-TE$_1$ and hybrid-TE$_2$ modes can be differentiated in wide trench waveguides, as shown in Figs. 10(h) and 10(i), their mode indices are close to each other in narrow trench waveguides, e.g., at $W_{btm} = 0$ in Fig. 10(a). The hybrid-TE$_1$ mode in a triangle trench waveguide ($W_{btm} = 0$) is illustrated in Fig. 10(d), and the hybrid-TE$_2$ mode in the same waveguide is shown in Fig. 10(e). One

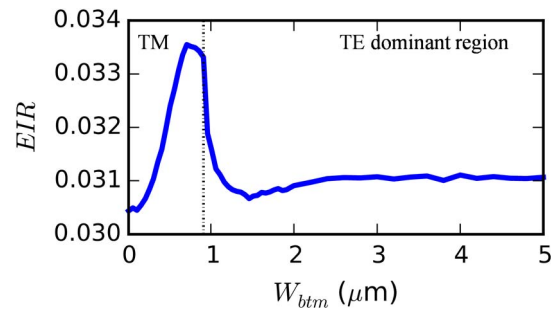should notice that the field orientation of the hybrid-TE$_2$ mode in the trench is along the y-axis in Fig. 10(e) as a result of the waveguide width reduction.

The TE modes in wide trench waveguides are of great interest in microfluidic sensing applications, especially when they are incorporated with plasmonic antennas [43]. Plasmonic antennas [or metal nanoparticles [21], shown as the inset in Fig. 10(a)] can be deposited on the trench waveguides to create local hot spots, which will give dramatic field enhancements [22]. Exciting these antennas efficiently requires launching the electric field parallel to the antenna plane; therefore, the TE mode will be in favor of coupling the waveguide mode to the antennas. However, the EIR of the TE fundamental mode could be smaller than the EIR of the quasi-TM mode, as presented in Fig. 11. For a top-etched trench waveguide with $T_{SiN} = 725$ nm, $H = 3$ μm, and water cladding, the maximum EIR of the fundamental mode occurs when W_{btm} is 0.7 μm and the corresponding fundamental mode is the quasi-TM mode. The EIR remains almost constant at 0.031 as W_{btm} continue increasing, and the fundamental mode becomes a TE mode. It is worth noting that the EIR curve shown here is not contradictory to what we investigated in Section 3.D, because the waveguides have two different geometries. In Section 3.D, the trench waveguides have top slabs which lead the mode to leak and thus cause the EIR to drop. Here, the top-etched trench waveguides have no leakage issue, and thereby no dimension restrictions. On the contrary, we can use the same conclusion presented in Section 3.D stating that thinner waveguides have a larger EIR and hence more light-matter interactions.

5. CONCLUSIONS

We numerically investigated the trench waveguides based on our previous experimental results. Both triangle and trapezoidal trench waveguides are studied and compared. To reduce the mode leakage into the top slab regions, an improved structure is put forward here. The reduction in the mode leakage opens the door to utilize the TE mode in wide trench waveguides. Although we use silicon nitride as the guiding material, this study can be applied to other guiding and cladding materials as well.

Compared to regular waveguides, trench waveguides have advantages and disadvantages. On the fabrication side, it is feasible to use conventional optical lithography to achieve sub-micron features in a low cost and large-scale manner, and the fabrication procedure can self-smooth the surface roughness, yielding low-loss propagation. In terms of nonlinear applications, triangle trench waveguides have small mode areas and manageable waveguide dispersions. Trench waveguides are also suitable for sensing applications because they can naturally combine a fluidic channel with an optical waveguide. Wide trapezoidal trench waveguides are favorable especially when combined with plasmonic antennas, because their TE modes can facilitate exciting antennas. However, wide waveguides may suffer large coupling losses due to mode mismatch. Therefore, the width of the trench should be designed carefully to cater to antenna fabrication and efficient mode coupling. For the top-etched waveguides, it is possible that the sidewall roughness caused by etching may affect the propagation loss, but the drawbacks need to be investigated thoroughly in future research. Since the waveguide fabrication relies on silicon etching properties, it also has some limitations, e.g., fabricating bending structures or coupling to regular waveguides. These restrictions will hamper trench waveguides from forming sophisticated telecommunication devices.

REFERENCES

1. K. E. Petersen, "Silicon as a mechanical material," Proc. IEEE **70**, 420–457 (1982).
2. L. P. Boivin, "Thin-film laser-to-fiber coupler," Appl. Opt. **13**, 391–395 (1974).
3. M. J. Wale and C. Edge, "Self-aligned flip-chip assembly of protonic devices with electrical and optical connections," IEEE Trans. Compon. Hybrids Manuf. Technol. **13**, 780–786 (1990).
4. S. Kaneko, M. Noda, K. Shibata, T. Aoyagi, H. Watanabe, T. Hatta, and K. Kasahara, "Novel fiber alignment method using a partially metal-coated fiber in a silicon V-groove," IEEE Photon. Technol. Lett. **12**, 645–647 (2000).
5. A. Priyadarshi, L. H. Fen, S. G. Mhaisalkar, V. Kripesh, and A. K. Asundi, "Fiber misalignment in silicon V-groove based optical modules," Opt. Fiber Technol. **12**, 170–184 (2006).
6. P. F. Heidrich, J. S. Harper, E. G. Lean, and H. N. Yu, "High density multichannel optical waveguides with integrated couplers," in *1975 International Electron Devices Meeting* (1975), pp. 602–603.
7. W.-T. Tsang, C.-C. Tseng, and S. Wang, "Optical waveguides fabricated by preferential etching," Appl. Opt. **14**, 1200–1206 (1975).
8. Y. Kokubun, T. Baba, and K. Iga, "Silicon optical printed circuit board for three-dimensional integrated optics," Electron. Lett. **21**, 508–509 (1985).
9. S. Chen and J. T. Boyd, "Integrated optical beam splitters formed in glass channel waveguides having variable weighting as determined by mask dimensions," IEEE J. Quantum Electron. **18**, 1072–1077 (1982).
10. R. Narendra and J. N. McMullin, "Single-mode, phosphorus-doped silica waveguides in silicon V-grooves," IEEE Photon. Technol. Lett. **5**, 43–46 (1993).
11. S. Kumar, R. I. MacDonald, and J. N. McMullin, "Low-loss multimode polymer waveguides with serial out-of-plane taps," in *Optical Fiber Communication* (Optical Society of America, 1992), paper FA8.
12. R. Narendra, I. N. McMullin, B. P. Keyworth, and R. I. MacDonald, "Dispensed dual-polymer waveguides in silicon V-grooves," in *Optical Microwave Interactions/Visible Semiconductor Lasers/Impact of Fiber Nonlinearities on Lightwave Systems/Hybrid Optoelectronic Integration and Packaging/Gigabit Networks, LEOS 1993 Summer Topical Meeting Digest* (IEEE, 1993), pp. H39–H40.
13. A. D'Alessandro, B. D. Donisi, R. Beccherelli, and R. Asquini, "Nematic liquid crystal optical channel waveguides on silicon," IEEE J. Quantum Electron. **42**, 1084–1090 (2006).
14. B. Bellini and R. Beccherelli, "Modelling, design and analysis of liquid crystal waveguides in preferentially etched silicon grooves," J. Phys. D **42**, 45111 (2009).
15. R. Asquini, D. Donisi, M. Trotta, A. d'Alessandro, B. Bellini, G. Gilardi, and R. Beccherelli, "Realization of a liquid crystal electrically controlled optical waveguide on micromachined silicon," Mol. Cryst. Liq. Cryst. **500**, 23–30 (2009).
16. A. d'Alessandro, R. Asquini, M. Trotta, G. Gilardi, R. Beccherelli, and I. C. Khoo, "All-optical intensity modulation of near infrared light in a liquid crystal channel waveguide," Appl. Phys. Lett. **97**, 93302 (2010).
17. D. Donisi, B. Bellini, R. Beccherelli, R. Asquini, G. Gilardi, M. Trotta, and A. d'Alessandro, "A switchable liquid-crystal optical channel waveguide on silicon," IEEE J. Quantum Electron. **46**, 762–768 (2010).
18. D. C. Zografopoulos, R. Asquini, E. E. Kriezis, A. d'Alessandro, and R. Beccherelli, "Guided-wave liquid-crystal photonics," Lab. Chip **12**, 3598–3610 (2012).
19. T.-J. Wang, C.-K. Chaung, W.-J. Li, T.-J. Chen, and B.-Y. Chen, "Electrically tunable liquid-crystal-core optical channel waveguide," J. Lightwave Technol. **31**, 3570–3574 (2013).
20. Y. Huang, Q. Zhao, L. Kamyab, A. Rostami, F. Capolino, and O. Boyraz, "Sub-micron silicon nitride waveguide fabrication using conventional optical lithography," Opt. Express **23**, 6780–6786 (2015).
21. Y. Huang, Q. Zhao, N. Sharac, R. Ragan, and O. Boyraz, "Highly nonlinear sub-micro silicon nitride trench waveguide coated with gold nanoparticles," Proc. SPIE **9503**, 95030H (2015).
22. Q. Zhao, C. Guclu, Y. Huang, F. Capolino, R. Ragan, and O. Boyraz, "Plasmon optical trapping using silicon nitride trench waveguides," J. Opt. Soc. Am. B **33**, 1182–1189 (2016).
23. P. M. Pelosi, P. Vandenbulcke, C. D. W. Wilkinson, and R. M. De La Rue, "Propagation characteristics of trapezoidal cross-section ridge optical waveguides: an experimental and theoretical investigation," Appl. Opt. **17**, 1187–1193 (1978).
24. J. G. Gallagher, "Mode dispersion of trapezoidal cross-section dielectric optical waveguides by the effective-index method," Electron. Lett. **15**, 734–736 (1979).
25. T. Miyamoto, "Numerical analysis of a rib optical waveguide with trapezoidal cross section," Opt. Commun. **34**, 35–38 (1980).
26. G. Yue-Jin, L. De-Jun, and A. D. Klemm, "Numerical investigation of a trapezoidal cross-section ridge optical waveguide," Numer. Methods Partial Differential Equations **12**, 307–314 (1996).
27. Q. Zhao, Y. Huang, R. Torun, S. Rahman, T. C. Atasever, and O. Boyraz, "Numerical investigation of silicon nitride trench waveguide," Proc. SPIE **9586**, 95860O (2015).
28. Y. Huang, *Integrated Optical Signal Processing Based on Optical Waveguides and Wavefront-Engineered Planar Devices* (University of California, 2014).
29. I. H. Malitson, "Interspecimen comparison of the refractive index of fused silica," J. Opt. Soc. Am. **55**, 1205–1209 (1965).
30. J. S. Levy, A. Gondarenko, M. A. Foster, A. C. Turner-Foster, A. L. Gaeta, and M. Lipson, "CMOS-compatible multiple-wavelength oscillator for on-chip optical interconnects," Nat. Photonics **4**, 37–40 (2010).
31. K. Ikeda, R. E. Saperstein, N. Alic, and Y. Fainman, "Thermal and Kerr nonlinear properties of plasma-deposited silicon nitride/silicon dioxide waveguides," Opt. Express **16**, 12987–12994 (2008).
32. G. P. Agrawal, *Nonlinear Fiber Optics* (Academic, 2007).
33. A. Boskovic, L. Gruner-Nielsen, O. A. Levring, S. V. Chernikov, and J. R. Taylor, "Direct continuous-wave measurement of n_2 in various types of telecommunication fiber at 155 μm," Opt. Lett. **21**, 1966–1968 (1996).
34. M.-C. Tien, J. F. Bauters, M. J. R. Heck, D. J. Blumenthal, and J. E. Bowers, "Ultra-low loss Si_3N_4 waveguides with low nonlinearity and

high power handling capability," Opt. Express **18**, 23562–23568 (2010).

35. C. J. Krückel, A. Fülöp, T. Klintberg, J. Bengtsson, P. A. Andrekson, and V. Torres-Company, "Linear and nonlinear characterization of low-stress high-confinement silicon-rich nitride waveguides," Opt. Express **23**, 25827–25837 (2015).

36. M. Dinu, F. Quochi, and H. Garcia, "Third-order nonlinearities in silicon at telecom wavelengths," Appl. Phys. Lett. **82**, 2954–2956 (2003).

37. T. M. Monro and H. Ebendorff-Heidepriem, "Progress in microstructured optical fibers," Annu. Rev. Mater. Res. **36**, 467–495 (2006).

38. J. P. Epping, M. Hoekman, R. Mateman, A. Leinse, R. G. Heideman, A. van Rees, P. J. M. van der Slot, C. J. Lee, and K.-J. Boller, "High confinement, high yield Si_3N_4 waveguides for nonlinear optical applications," Opt. Express **23**, 642–648 (2015).

39. K. Luke, A. Dutt, C. B. Poitras, and M. Lipson, "Overcoming Si_3N_4 film stress limitations for high quality factor ring resonators," Opt. Express **21**, 22829–22833 (2013).

40. A. G. Griffith, R. K. W. Lau, J. Cardenas, Y. Okawachi, A. Mohanty, R. Fain, Y. H. D. Lee, M. Yu, C. T. Phare, C. B. Poitras, A. L. Gaeta, and M. Lipson, "Silicon-chip mid-infrared frequency comb generation," Nat. Commun. **6**, 6299 (2015).

41. J. Kim, O. Boyraz, J. H. Lim, and M. N. Islam, "Gain enhancement in cascaded fiber parametric amplifier with quasi-phase matching: theory and experiment," J. Lightwave Technol. **19**, 247–251 (2001).

42. Y. Huang, E.-K. Tien, S. Gao, S. K. Kalyoncu, Q. Song, F. Qian, and O. Boyraz, "Quasi-phase matching in SOI and SOS based parametric wavelength converters," Proc. SPIE **8120**, 81200F (2011).

43. M. L. Juan, M. Righini, and R. Quidant, "Plasmon nano-optical tweezers," Nat. Photonics **5**, 349–356 (2011).